Supplementary information (ESI) for Journal of Materials Chemistry

High-temperature solvent-free sulfidation of MoO3 confined in a polypyrrole shell: MoS2 nanosheets encapsulated in a nitrogen, sulfur dual-doped carbon nanoprism for efficient lithium storage

Ying Liu[a], Jixin Zhu[b], Jingsan Xu[c], Siliang Liu[a], Le Li[a], Chao Zhang[a,*], Tianxi Liu[a,*]

[a] State Key Laboratory for Modification of Chemical Fibers and Polymer Materials, College of Materials Science and Engineering, Donghua University, Shanghai 201620, P. R. China

[b] Key Laboratory of Flexible Electronics (KLOFE) & Institute of Advanced Materials (IAM), Jiangsu National Synergetic Innovation Center for Advanced Materials (SICAM), Nanjing Tech University (Nanjing Tech), 30 South Puzu Road, Nanjing 211816, P. R. China

[c] School of Chemistry, Physics and Mechanical Engineering, Queensland University of Technology, Brisbane, QLD 4001, Australia

* E-mail: czhang@dhu.edu.cn (C. Zhang)

* E-mail: txliu@fudan.edu.cn or txliu@dhu.edu.cn (T. X. Liu)

Electronic Supplementary Information

Figure captions:

Fig. S1 SEM image of MoO_3 at a low magnification.
Fig. S2 SEM and TEM images of MoO_3@PPy prepared with the pyrrole/MoO_3 mass ratios of a, b) 4/10 and c, d) 1/10, respectively, during in-situ polymerization.
Fig. S3 XRD patterns of MoO_3, MoO_3@PPy and PPy.
Fig. S4 SEM images of MoS_2@NSC-2 after grinding at a) low and b) high magnifications, respectively.
Fig. S5 a) XPS survey spectrum and b) elemental composition of MoS_2@NSC-2.
Fig. S6 SEM and TEM images of a,b) MoS_2@NSC-1 and c,d) MoS_2@NSC-3.
Fig. S7 XRD patterns of MoO_3@PPy treated at different sulfidation temperatures.
Fig. S8 SEM images of neat MoS_2 at a) low and b) high magnifications, respectively.
Fig. S9 SEM images of neat PPy at a) low and b) high magnifications, respectively.
Fig. S10 a, b) SEM and c, d) TEM images of NSC at low and high magnifications, respectively.
Fig. S11 Raman spectra of MoS_2, MoS_2@NSC and NSC.
Fig. S12 XRD patterns of NSC, MoS_2@NSC, and MoS_2.
Fig. S13 TGA curves of MoS_2, NSC, MoO_3 and MoS_2@NSC.
Fig. S14 CV curves of neat MoS_2 electrode.
Fig. S15 Nyquist plots of MoS_2 and MoS_2@NSC at the frequency range between 100 kHz and 0.01 Hz.
Fig. S16 TEM images of a,b) MoS_2@NSC and c, d) MoS_2 electrodes after 300 cycles at low and high magnifications, respectively.
Fig. S17 Electrochemical characterizations of the MoS_2@NSC-1 electrode for LIBs: a) discharge-charge voltage profiles at a current density of 0.1 A g^{-1}, b) rate capability, and c) cycling performance at a current density of 0.1 A g^{-1}.
Fig. S18 Electrochemical characterizations of the MoS_2@NSC-3 electrode for LIBs: a) discharge-charge voltage profiles at a current density of 0.1 A g^{-1}, b) rate capability, and c) cycling performance at a current density of 0.1 A g^{-1}.
Fig. S19 Electrochemical characterizations of the NSC electrode for LIBs: a) discharge-charge voltage profiles at a current density of 0.1 A g^{-1}, b) rate capability, and c) cycling performance at a current density of 0.1 A g^{-1}.
Table S1. Elemental analysis of NSC and MoS_2@NSC-2.
Table S2. Performance comparison of MoS_2-based materials for lithium storages.

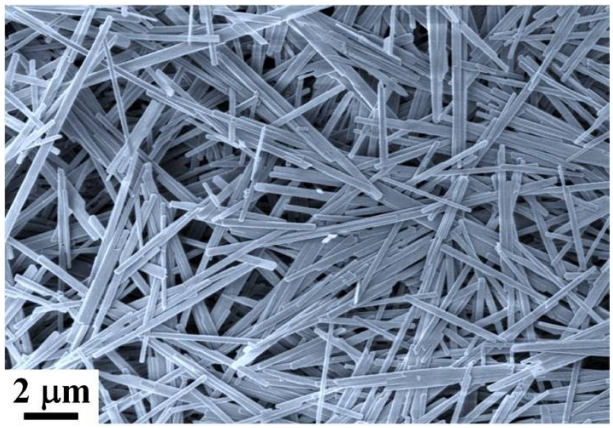

Fig. S1 SEM image of MoO_3 at the low magnification.

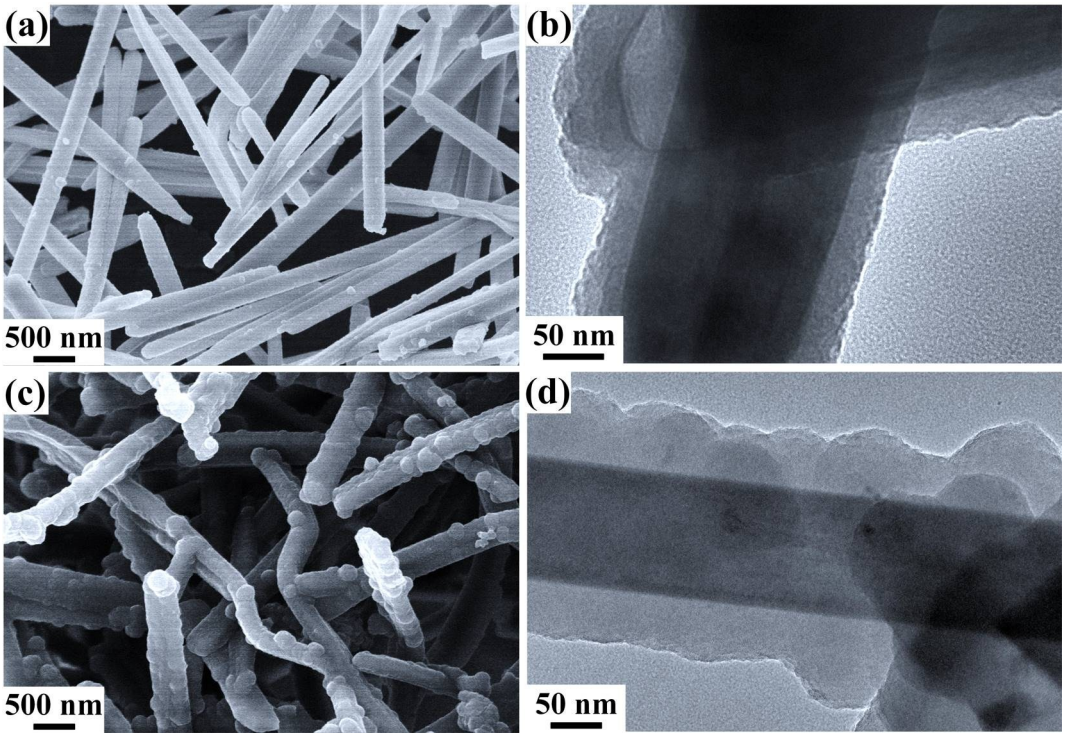

Fig. S2 SEM and TEM images of MoO_3@PPy prepared with the pyrrole/MoO_3 mass ratios of a, b) 4/10 and c, d) 1/10, respectively, during in-situ polymerization.

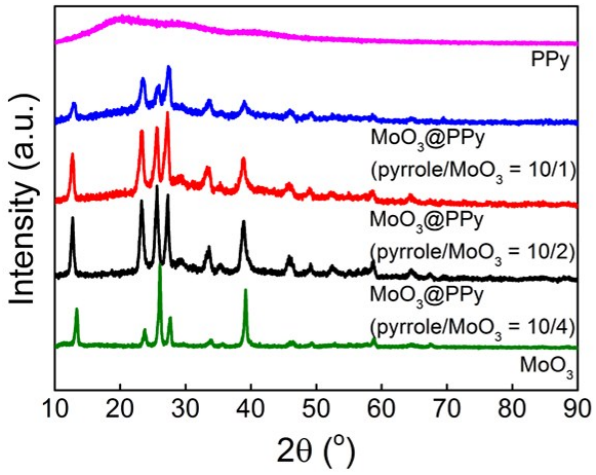

Fig. S3 XRD patterns of MoO_3, MoO_3@PPy and PPy.

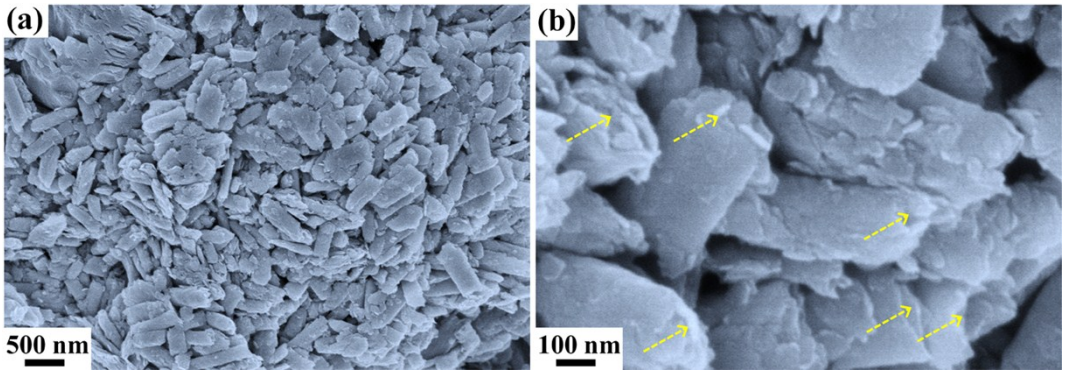

Fig. S4 SEM images of MoS_2@NSC-2 after grinding at a) low and b) high magnifications, respectively.

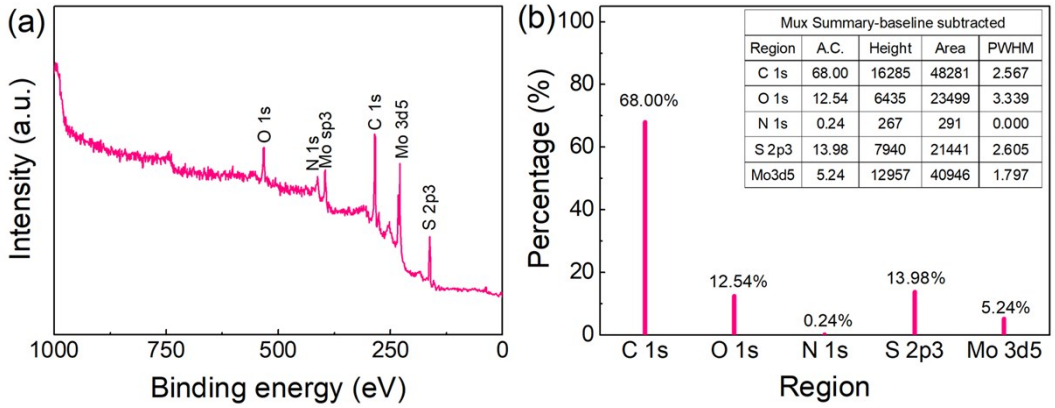

Fig. S5 a) XPS survey spectrum and b) elemental composition of MoS_2@NSC-2.

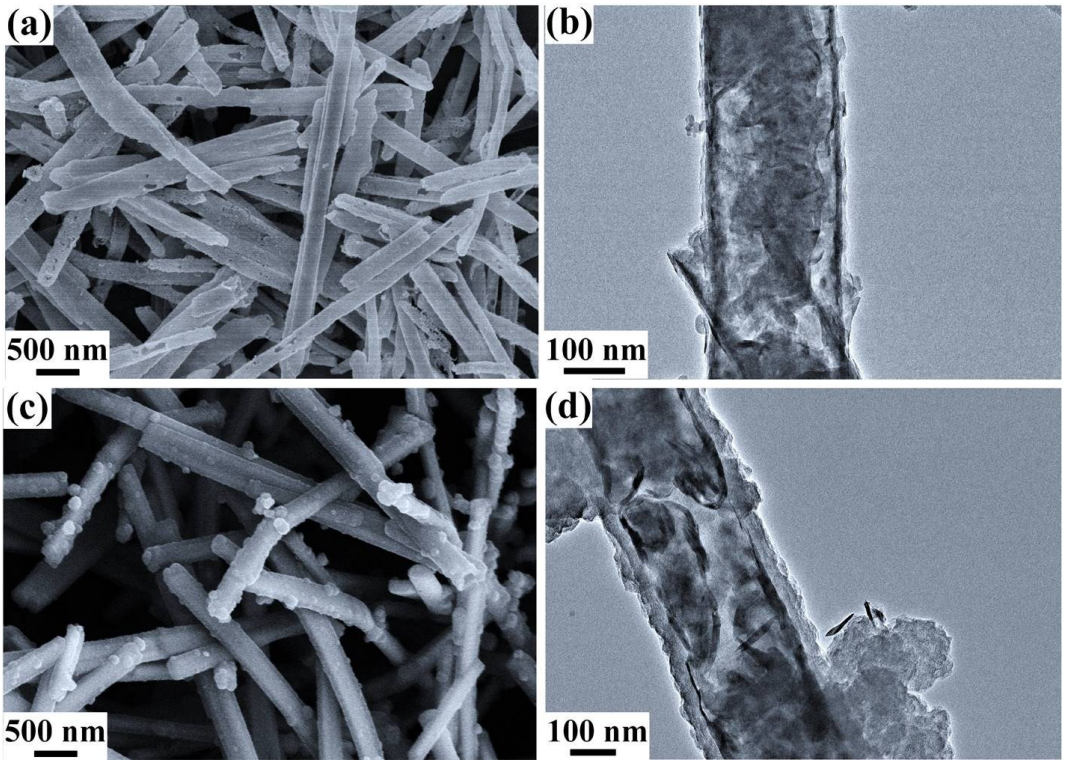

Fig. S6 SEM and TEM images of a,b) MoS_2@NSC-1 and c,d) MoS_2@NSC-3.

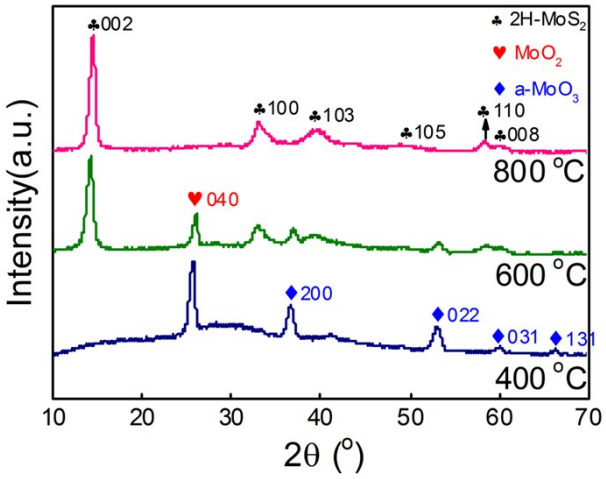

Fig. S7 XRD patterns of MoO_3@PPy treated at different sulfidation temperatures.

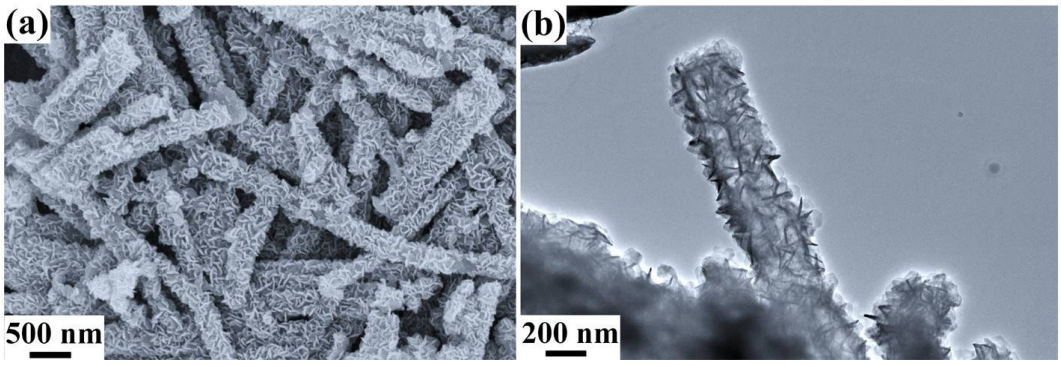

Fig. S8 SEM images of neat MoS_2 at a) low and b) high magnifications, respectively.

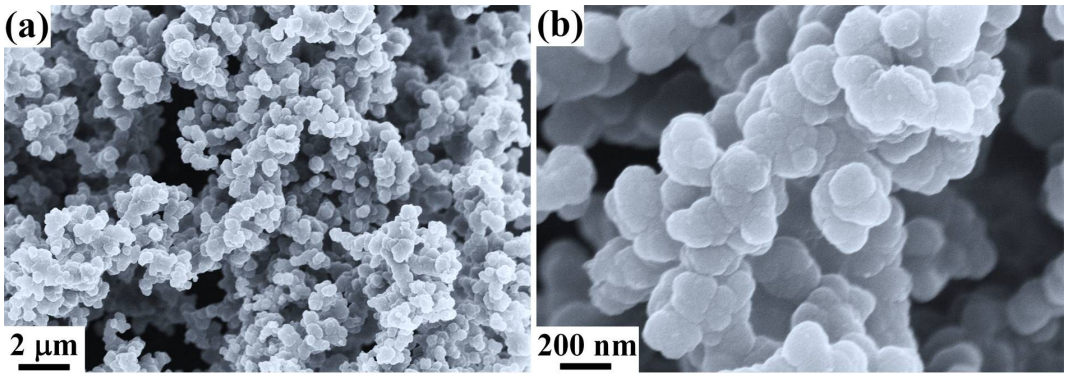

Fig. S9 SEM images of neat PPy at a) low and b) high magnifications, respectively.

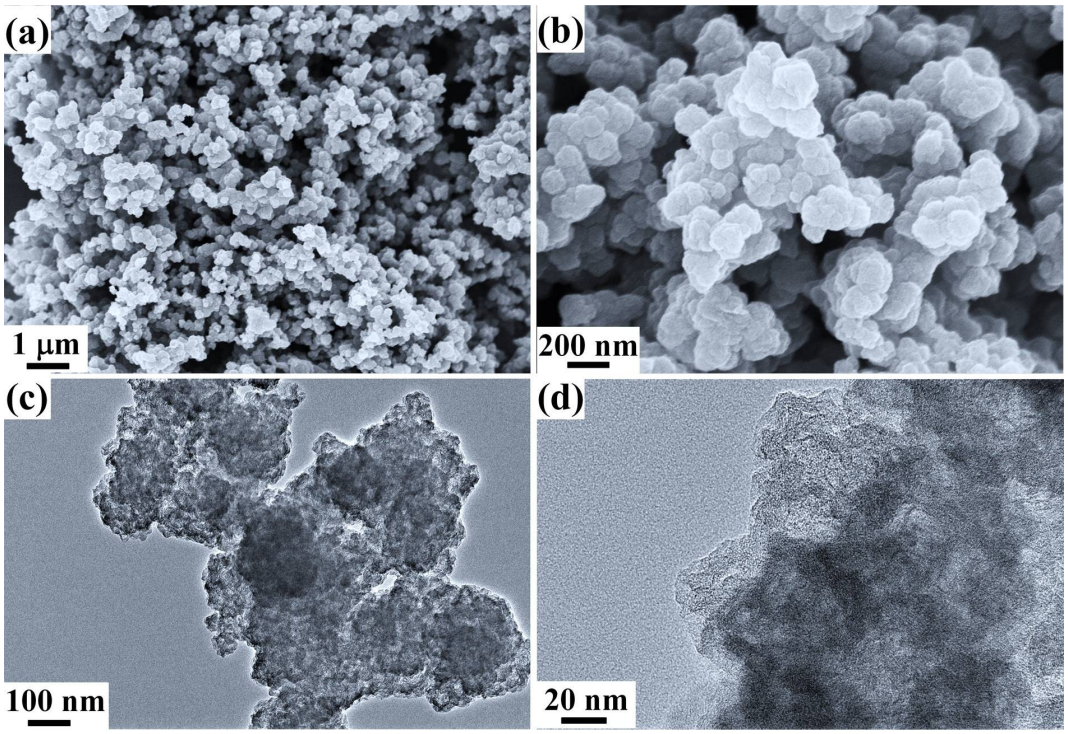

Fig. S10 a, b) SEM and c, d) TEM images of NSC at low and high magnifications, respectively.

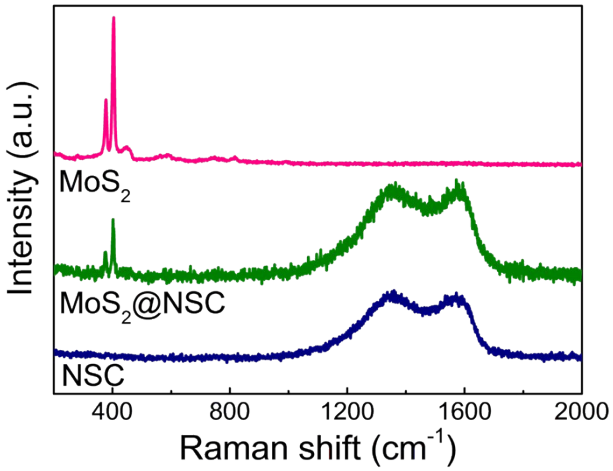

Fig. S11 Raman spectra of MoS_2, MoS_2@NSC and NSC. The hexagonal layered structure of h-MoS_2 are evidenced by two Raman peaks at 383 cm^{-1} (E_{12g}: first-order Raman active modes mode) and 408 cm^{-1} (A_{1g}: in-plane vibrational mode within sulfur-molybdenum-sulfur layer). The Raman spectrum of MoS_2@NSC exhibits two broad bands at 1360 cm^{-1} (D band) and 1598 cm^{-1} (G band), besides typical peaks derived from MoS_2, indicating the formation of carbon materials within the MoS_2@NSC.

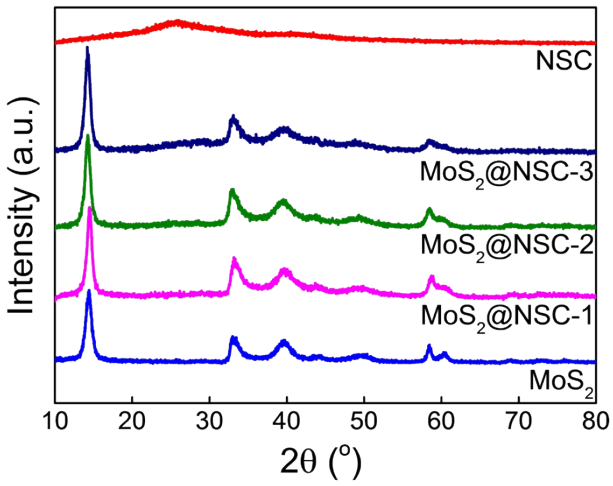

Fig. S12 XRD patterns of NSC, MoS_2@NSC, and MoS_2.

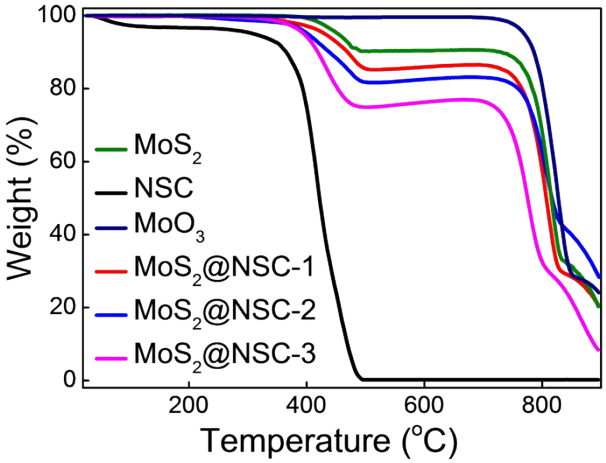

Fig. S13 TGA curves of MoS_2, NSC, MoO_3 and MoS_2@NSC.

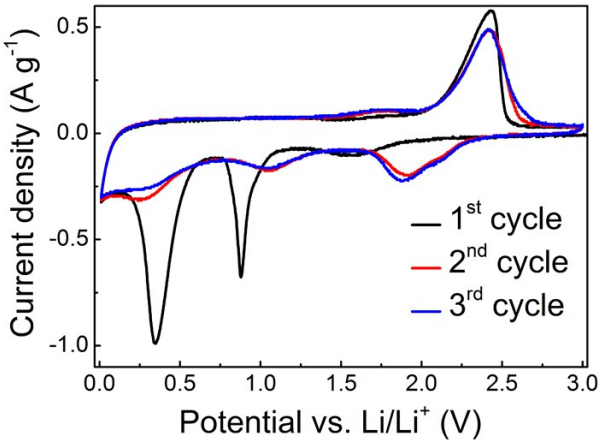

Fig. S14 CV curves of neat MoS_2 electrode.

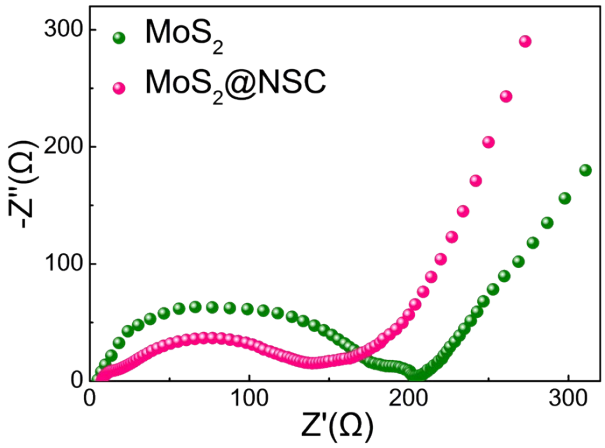

Fig. S15 Nyquist plots of MoS_2 and MoS_2@NSC at the frequency range between 100 kHz and 0.01 Hz.

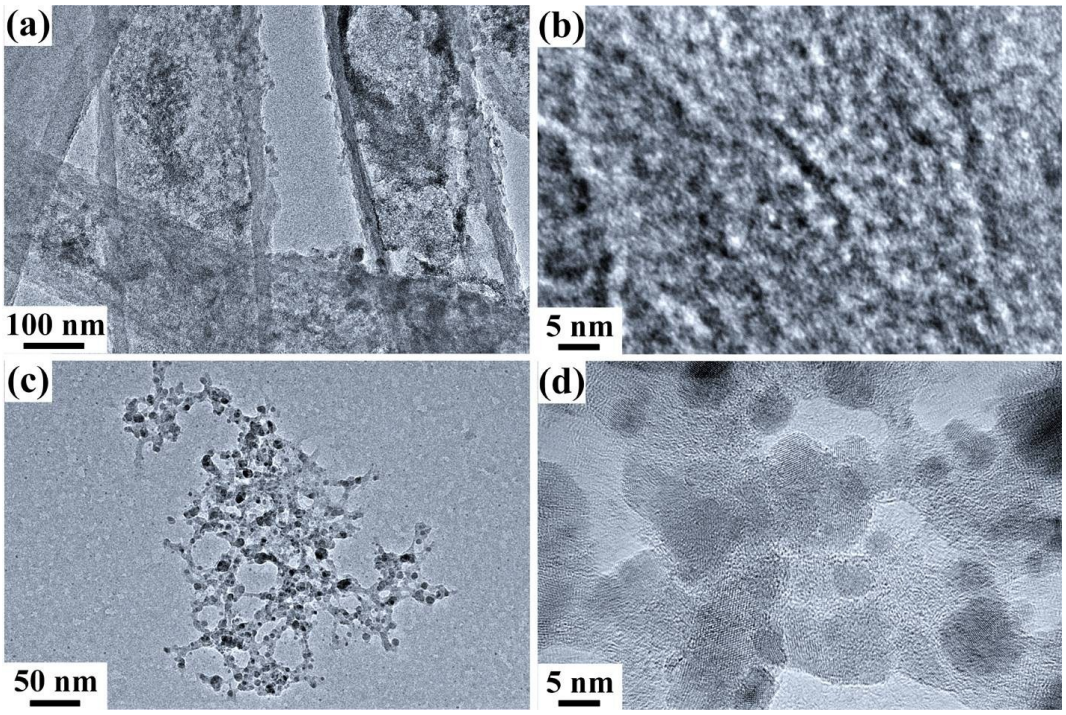

Fig. S16 TEM images of a,b) MoS_2@NSC and c, d) MoS_2 electrodes after 300 cycles at low and high magnifications, respectively.

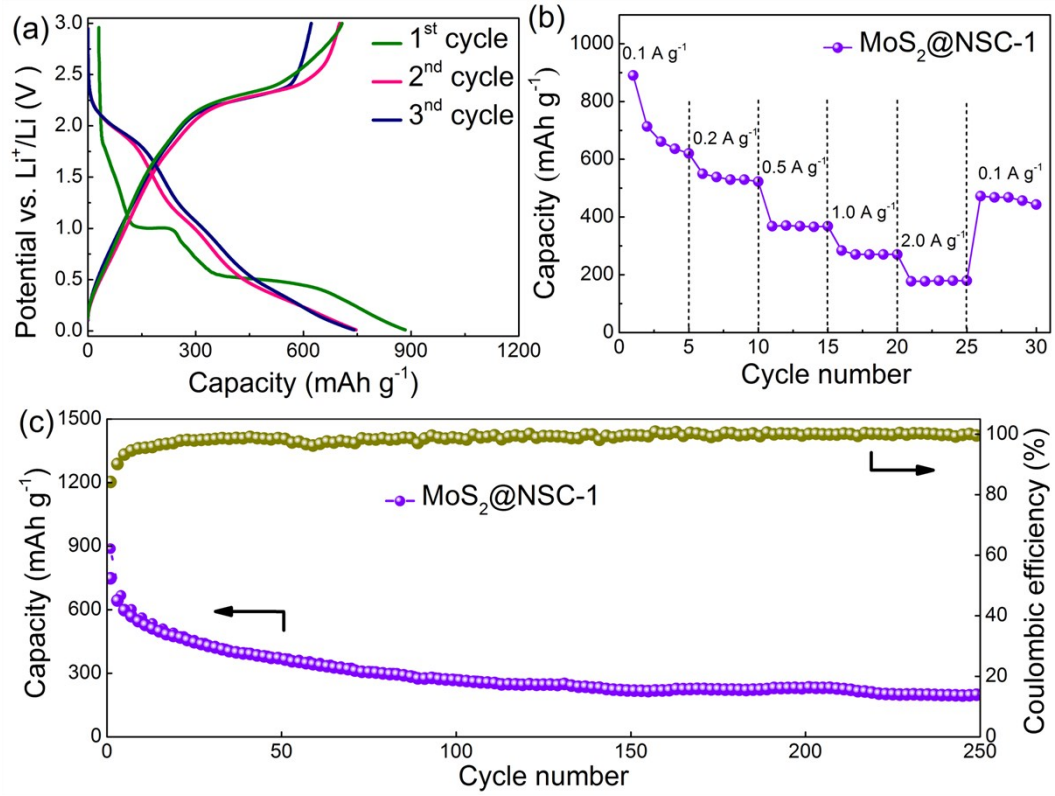

Fig. S17 Electrochemical characterizations of the MoS_2@NSC-1 electrode for LIBs: a) discharge-charge voltage profiles at a current density of 0.1 A g^{-1}, b) rate capability, and c) cycling performance at a current density of 0.1 A g^{-1}. Although the MoS_2@NSC-1 electrode exhibits a high CE of 80.2%, the electrode delivers relatively low discharge capacity of only 883 mA h g^{-1} and poor cycling stability with capacity retention of 41.6% after 50 cycles. The poor electrochemical performances of MoS_2@NSC-1 are due to the agglomeration of non-capsulated MoS_2 without the perfect confinement by outer NSC.

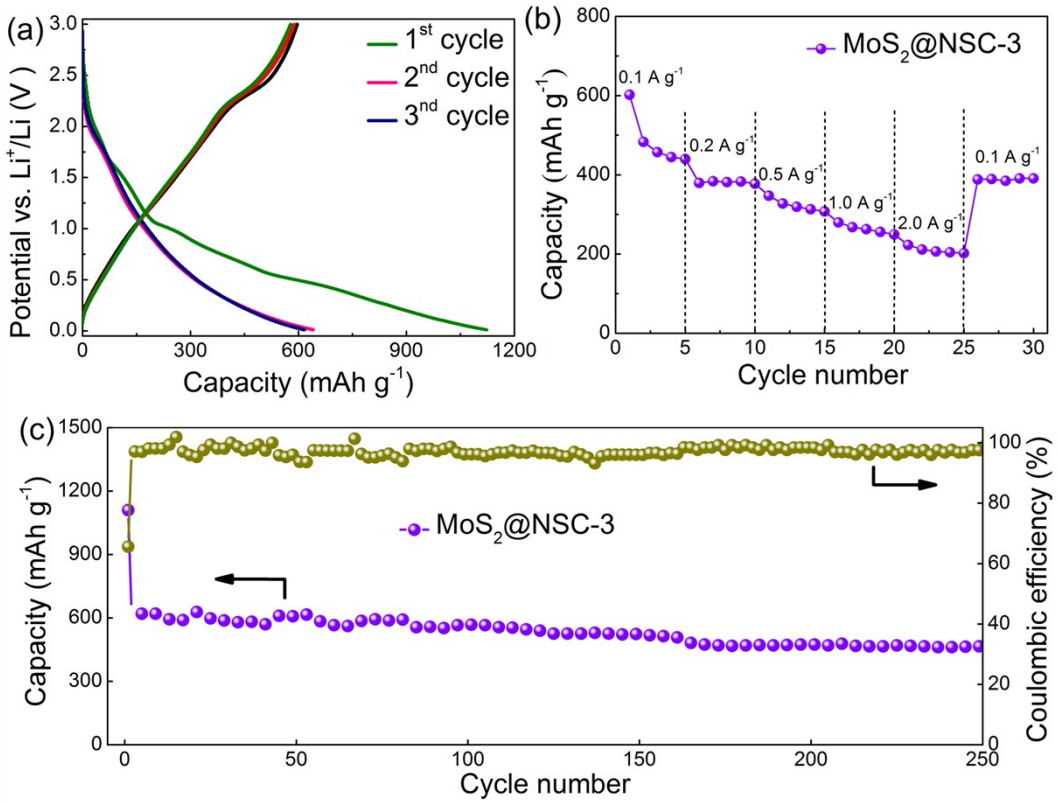

Fig. S18 Electrochemical characterizations of the MoS_2@NSC-3 electrode for LIBs: a) discharge-charge voltage profiles at a current density of 0.1 A g^{-1}, b) rate capability, and c) cycling performance at a current density of 0.1 A g^{-1}. The MoS_2@NSC-3 electrode delivers a high discharge capacity of 1124 mA h g^{-1} and satisfying cycling stability with a capacity of 470.6 mA h g^{-1} after 250 cycles. However, the specific capacity is much lower compared to h- MoS_2@NSC-2 sample because lower content of high-capacity MoS_2 within the MoS_2@NSC-3.

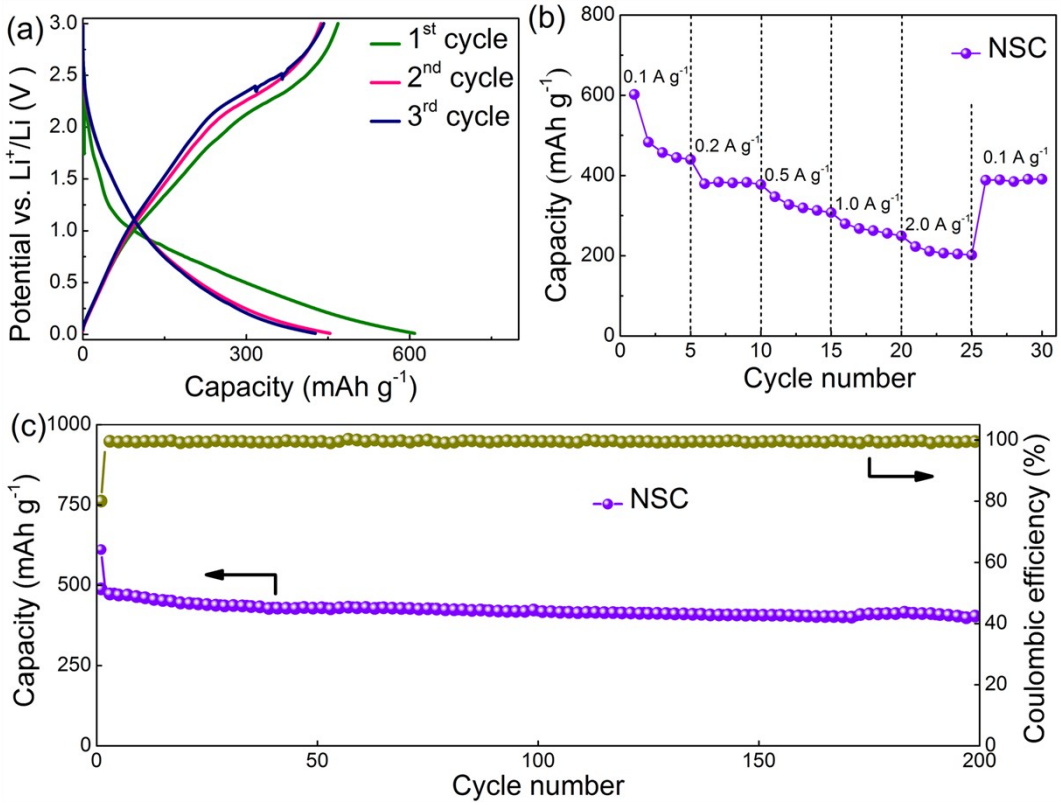

Fig. S19 Electrochemical characterizations of the NSC electrode for LIBs: a) discharge-charge voltage profiles at a current density of 0.1 A g^{-1}, b) rate capability, and c) cycling performance at a current density of 0.1 A g^{-1}. It can be seen from the voltage profiles of the first cycle that the NSC shows a typical discharge-charge characteristic of disordered carbon. The NSC electrode delivers a first-cycle discharge capacity of 611 mA h g^{-1}. Note that the reversible capacity of the NSC electrode reaches 403 mA h g^{-1} after 200 cycled, which is higher than that of the state-of-the-art anode material graphite (~ 342 mA h g^{-1}).

Table S1. Elemental analysis of NSC and MoS_2@NSC-2.

Samples	C	N	S
NSC	89.2 wt%	2.6 wt%	2.1 wt%
MoS2@NSC-2	9.0 wt%	0.2 wt%	36.5%

Table S2. Performance comparison of MoS_2-based materials for lithium storages.

Materials	Methods	Capacity at 0.1 A g^{-1} (mA h g^{-1})	Ref.
MoS_2@polyaniline nanowires	Solvothermal	1063	[1]
MoS_2@graphene networks	CVD	1222	[2]
Few-layer MoS_2 on carbon nanosheet	CVD	1161	[3]
MoS_2@carbon microspheres	Solvothermal	1054	[4]
MoS_2@carbon microtube	Solvothermal	752	[5]
MoS_2 nanothorns@CNT	CVD	982	[6]
MoS_2@rGO	Solvothermal	1412	[7]
Tubular MoS_2 @CNT	Solvothermal	1320	[8]
MoS_2@carbon nanofiber	Solvothermal	846	[9]
MoS_2/graphene aerogels	Solvothermal	1360	[10]
MoS_2@NSC nanoprisms	**Solvent-free sulfidation**	**960**	**This work**

References

1. L. C. Yang, S. N. Wang, J. J. Mao, J. W. Deng, Q. S. Gao, Y. Tang and O. G. Schmidt, *Adv. Mater.*, 2013, **25**, 1180-1184.
2. X. Cao, Y. Shi, W. Shi, X. Rui, Q. Yan, J. Kong and H. Zhang, *Small*, 2013, **9**, 3433-3438.
3. J. Zhou, J. Qin, X. Zhang, C. Shi, E. Liu, J. Li, N. Zhao and C. He, *ACS Nano*, 2015, **9**, 3837-3848.
4. F. Sun, Y. Wei, J. Chen, D. Long, L. Ling, Y. Li and J. Shi, *Nanoscale*, 2015, **7**, 13043-13050.
5. Y. Teng, M. Mo and P. Lv, *Mater. Lett.*, 2017, **209**, 396-399.
6. Z. Zhang, H. Zhao, Y. Teng, X. Chang, Q. Xia, Z. Li, J. Fang, Z. Du, Konrad, x. a and wierczek, *Adv. Energy Mater.*, 2017, DOI: 10.1002/aenm.201700174.
7. X. Hu, Y. Li, G. Zeng, J. Jia, H. Zhan and Z. Wen, *ACS Nano*, 2018, DOI: 10.1021/acsnano.7b08161.
8. Y. M. Chen, X. Y. Yu, Z. Li, U. Paik and X. W. Lou, *Sci. Adv.*, 2016, **2**, 1600021.
9. J.-G. Wang, R. Zhou, D. Jin, K. Xie and B. Wei, *Electrochim. Acta*, 2017, **231**, 396-402.
10. P. He, K. Zhao, B. Huang, B. Zhang, Q. Huang, T. Chen and Q. Zhang, *J. Mater. Sci.*, 2018, **53**, 4482-4493.